Materials Advances

ROYAL SOCIETY OF CHEMISTRY

PAPER

View Article Online
View Journal | View Issue

Open Access Article. Published on 13 September 2023. Downloaded on 1/31/2026 1:12:25 PM.
This article is licensed under a Creative Commons Attribution-NonCommercial 3.0 Unported Licence.

Check for updates

Cite this: *Mater. Adv.*, 2023, 4, 5160

Fabrication of highly efficient encapsulated SnO_2@alginate beads as regenerative nanosorbents for anionic dye pollutants removal from aqueous solution†

Shikha Jyoti Borah,[a] Akanksha Gupta,[b] Kashyap Kumar Dubey[c] and Vinod Kumar *[a]

Received 29th August 2023,
Accepted 12th September 2023

DOI: 10.1039/d3ma00615h

rsc.li/materials-advances

Nano-adsorbents are emerging as potential candidates for the treatment of toxic organic pollutants. In this context, spherical SnO_2 nanoparticles (NPs) are synthesized through a facile hydrothermal method without the usage of toxic chemical precursors, which is confirmed through PXRD, TEM, FTIR, and Raman spectroscopy. SEM imaging was used to confirm the spherical morphology of the NPs. These NPs when applied as nano-adsorbents demonstrate the ability to remove anionic dyes from aqueous solution. In particular, 0.1 g/100 mL SnO_2 NPs exhibit 95.96% Congo red (CR) removal efficiency from its aqueous solution within an exposure time of 1 min. Primary driving forces of adsorption can be attributed to electrostatic attraction and hydrogen bonding. Raman spectra confirmed the presence of oxygen vacancies which can be a major factor for their high adsorption efficiency. The adsorption process for CR dye fitted felicitously with pseudo-second order kinetics indicating chemisorption and the Langmuir model indicating CR monolayer formation on the nano-adsorbent. The maximum adsorption capacity is estimated to be 961.5 mg g^{-1}. Finally, the possibility of metal leaching has been addressed through encapsulation of SnO_2 NPs within sodium alginate crosslinked by $CaCl_2$, which also exhibited nearly 75% adsorption efficiency after an exposure time of 5 min, with successful regeneration. In addition to adsorption capability toward CR dye, SnO_2@SA also exhibited moderate adsorption efficiencies towards eosin yellow, orange G, and methyl orange dyes. This study demonstrates SnO_2 NPs as a potential nano-adsorbent for treatment of toxic effluents through a sustainable, facile and economical method.

1. Introduction

On an industrial basis, each year, approximately 7×10^5 tons of wide ranges of synthetic dyes and pigments are used.[1] The printing and textile industry releases industrial wastewater after primary treatment, which does not efficiently remove the dyes, thereby resulting in the contamination of water bodies.[2,3] The release of untreated effluents containing a high concentration of dyes into the aquatic environment endangers both the ecological environment and human health. Due to their toxicity, mutagenicity, and carcinogenicity, azo dyes like Direct Blue15, Congo Red, and Direct Red 2 are recognized as hazardous to human health.[4,5] Particularly, Congo red (CR) dye, which is used extensively in the textile sector, has a strong affinity for cellulose fibers.[6] Numerous methods have been investigated to reduce dye pollution in wastewater, each with various benefits and drawbacks. Some of these methods include biodegradation,[7] photodegradation,[8] membrane separation,[9] and adsorption.[2,10] Adsorption is acknowledged as a viable method due to its simplicity, affordability, and sustainability. Micro-pollutants (such as dyes) can be removed from industrial effluents using the technique of adsorption. Adsorbents used in this technique should be easy to use and store, have good mechanical strength, possess the right pore structure and surface chemical composition, have significant capacity for adsorbing the adsorbate, and be highly recyclable and re-usable for economic reasons.[10]

Various adsorbents related to the environmental remediation of dyes in textile effluents have been explored in a wide range of publications.[2,10–14] However, SnO_2 nanoparticles (NPs) have attracted significant interest in multiple industries because of

[a] *Special Centre for Nano Science, Jawaharlal Nehru University, Delhi 110067, India. E-mail: kumarv@mail.jnu.ac.in, vinod7674@gmail.com*
[b] *Department of Science and Technology, Technology Bhavan, Delhi-110016, India*
[c] *School of Biotechnology, Jawaharlal Nehru University, Delhi 110067, India*

† Electronic supplementary information (ESI) available. See DOI: https://doi.org/10.1039/d3ma00615h

© 2023 The Author(s). Published by the Royal Society of Chemistry

Open Access Article. Published on 13 September 2023. Downloaded on 1/31/2026 1:12:25 PM.
This article is licensed under a Creative Commons Attribution-NonCommercial 3.0 Unported Licence.

Table 1 Investigations related to SnO_2 based nanomaterials for mitigation of CR dye *via* two facile methods (adsorption and photocatalytic degradation)

Nanomaterial	Synthesis	Removal technique	Removal efficiency (%)	Contact time (min)	Ref.
SnO_2	Sol–gel method	Adsorption	84.41	60	17
Fe_2O_3–SnO_2 nanorods	Wet-chemical method	Adsorption	99.9	30	26
SnO_2	*Simarouba glauca* leaf extract	Photocatalytic degradation	80	150	27
ZnO/SnO_2	Electrospun method	Photocatalytic degradation	78.29	60	28
SnO_2	Precipitation and calcination	Photocatalytic degradation	100	97	29
SnO_2/chitosan	Chemical precipitation	Photocatalytic degradation	95	60	30
SnO_2 nanosheets	Hydrothermal method	Photocatalytic degradation	96	55	31

their intriguing physicochemical features.[15] SnO_2 is an n-type semiconducting oxide having a wide band gap and it possesses high resistance to photocorrosion.[16] SnO_2 NPs can be prepared through various routes such as sol–gel,[17] hydrothermal,[18] microemulsion,[19] and the solvothermal method.[20] Among the available methods, the hydrothermal technique has emerged as a highly versatile and conventional choice, garnering popularity in industrial applications owing to its straightforward methodology, high yield, cost-effectiveness and suitability for moderate-temperature processes.[21] Moreover, this method is well-recognized for its ability to produce NPs with desired size and shape, well-crystalized products, and NPs exhibiting high crystallinity.[22] SnO_2 has been investigated as a potential material with numerous unique surface features, such as luminescence and photocatalytic activity, over the past ten years.[15,23] Due to its high chemical stability and unique physico-chemical properties, it has been utilized in various applications such as sensors,[24] photocatalytic degradation,[15] thermoluminescence[25] and many others.

Table 1 presents the various studies carried out for removal and degradation of CR dye using SnO_2 based nanomaterials *via* two common routes, namely adsorption and photocatalytic degradation. Adsorbents are typically utilized as a fine powder, and the difficulty of separating the adsorbent from the effluent may result in sorbent loss. Besides this, metal leaching can also pose as an inevitable subsequence of using the powder form of adsorbents. Encapsulating nanomaterials in alginate beads is a clever solution to this challenge. Alginate is a polymer derived from brown seaweed. It has substantial advantages, including accessibility, relatively inexpensiveness, non-toxicity, biocompatibility, and biodegradability.[32] Nanomaterial-alginate beads have garnered attention due to the combined properties and advantages of their constituents.[6,33–38]

In this study, the efficiency of hydrothermally produced SnO_2 NPs for CR dye removal from its aqueous solution is meticulously evaluated. Additionally, the encapsulation of SnO_2 NPs in sodium alginate (SA) beads, their use as nano-adsorbents, as well as their capacity to demonstrate regenerative cycles have been explored. Three primary approaches were used to conduct this study: sustainability, viability, and cost-effectiveness. To completely assess their adsorption effectiveness, a range of operational parameters, including pH, contact time, the amount of adsorbent, and dye concentrations, have been studied. To ascertain the adsorption mechanisms, the adsorption isotherms and kinetics were also investigated. SnO_2 encapsulated within SA (SnO_2@SA) beads highlights the reduced likelihood of post-adsorption metal leaching while also illuminating the practical applicability of the synthesized NPs. In its entirety, the utilization of SnO_2 NPs for dye removal and their encapsulation within alginate beads constitute a fascinating approach that provides numerous advantages over traditional techniques, including the ease of adsorbent separation from the treated wastewater, the adsorbent's increased stability and reusability, and the nanoparticles' decreased toxicity. This research is intended to help establish an effective and sustainable process for treating dye wastewater, which could have major positive effects on the environment, water industry and economy.

2. Materials and method

2.1 Materials

The materials $SnCl_2{\cdot}2H_2O$ (tin(II) chloride dihydrate, 98–103% purity), $CaCl_2$ (calcium dichloride, 98% purity), CH_3OH (methanol having >99% purity), ethanol and acetone were purchased from Merck Chemicals. H_2O_2 (hydrogen peroxide, 30% w/v purity), Congo red, eosin yellow, methyl orange and orange G were purchased from Thermo Fisher Scientific. Sodium alginate was purchased from High Purity Laboratory Chemical Pvt. Ltd. All chemicals and solvents used in the experiments were of analytical grade.

2.2 Synthesis of nanoparticles

SnO_2 was prepared through a facile hydrothermal reaction. In a clean and dry vessel, 40 mL methanolic solution of 0.11 M $SnCl_2{\cdot}2H_2O$ was used. To this, 10 mL of hydrogen peroxide was added. The solution was autoclaved at 150 °C for 15 hours. Thereafter, the sample was washed numerous times with distilled water and then with methanol for removal of any residual impurities. Finally, the sample was oven dried at 60 °C and ground in a mortar and pestle to obtain a white homogeneous SnO_2 NP powder.

2.3 Synthesis of alginate beads

A 3% solution of sodium alginate was prepared which was continuously stirred for 2 hours to form a homogeneous viscous gel. 100 mL of 0.05 M $CaCl_2$ solution was prepared in a separate beaker. This was followed by dropwise addition of alginate gel to the $CaCl_2$ solution which led to the formation of light brown spherical beads.[39,40] The beads were kept immersed in $CaCl_2$ overnight, and then washed with distilled water several times. Finally, the beads were partially oven dried at 80 °C to remove excess water and then utilized for adsorption studies.

Open Access Article. Published on 13 September 2023. Downloaded on 1/31/2026 1:12:25 PM.
This article is licensed under a Creative Commons Attribution-NonCommercial 3.0 Unported Licence.

2.4 Encapsulation of SnO_2 in alginate beads

First, 3% solution of sodium alginate was prepared. To the viscous gel, varying concentrations of SnO_2 NPs (0.1 g, 0.2 g and 0.5 g) were added with continuous stirring for 2 hours to form a homogeneous viscous gel. This was followed by preparation of 0.05 M $CaCl_2$ solution. The viscous gel was dropwise added to $CaCl_2$ solution to form spherical white colored SnO_2@SA beads. Further, these beads were kept overnight in $CaCl_2$ solution for hardening, which was followed by washing with distilled water. Finally, they were partially oven dried at 80 °C to remove excess water for further usage in adsorption studies.

2.5 Adsorption of anionic dyes

All the batch experiments, for adsorption studies, were carried out at room temperature. First, tests were conducted in 100 mL glass beakers with varying dye concentrations (5–60 μM) using the powder form of SnO_2 NPs. Similar batch experiments were carried out for investigating the efficiency of SnO_2@SA beads in 5 μM aqueous solutions of anionic dyes. 5 mL aliquots of solution were collected at regular time intervals, and then centrifuged to remove the nano-adsorbent for further analysis on a UV-Visible spectrophotometer. For pH studies, 1 M HCl/NaOH solutions were used. For carrying out desorption studies, chemical regeneration was carried out using 15 mL of various eluents such as methanol, ethanol, acetone, and dil. HCl.

2.6 Instruments

The crystalline structure of the synthesized NPs was characterized by PXRD using a scan rate of 1° min^{-1} for 2θ range from 5° to 70° in a Rigaku Miniflex 600 (Japan) X-ray diffractometer (λ = 1.5406 Å). For determining the sample morphology and elemental composition, SEM images and EDX spectra were obtained from a SEM (JEOL) coupled with an EDX detector. TEM images were obtained from a Tecnai G2 20 S-TWIN TEM. FTIR and Raman spectra were recorded using a Shimadzu instrument and an EnSpectr^{+}R532 spectrometer (λ = 532 nm), respectively. Sn detection was carried out on Agilent ICP-MS 7900. UV-Visible spectra were recorded using a UV-Visible spectrophotometer (PG Instruments, India).

3. Results and discussion

3.1 X-ray diffraction

The crystallographic studies of SnO_2 NPs have been confirmed by PXRD. Fig. 1(a) depicts the obtained XRD pattern. NPs are confirmed to have a rutile structure having tetragonal phase with space group $P4_2/mnm$. The concluded data are in agreement with JCPDS file no. 41-1445. In addition to this, the diffraction peaks have been indexed to the characteristic planes (110), (101), (200), (210), (211), (002), and (310). The highest relative intensity peak was determined for (101) and (210) planes. The average crystallite NP size has been determined to be approximately 3–5 nm using the Debye–Scherrer equation. No characteristic peak was additionally observed, depicting the purity of the synthesized NPs. Thus, it can be concluded

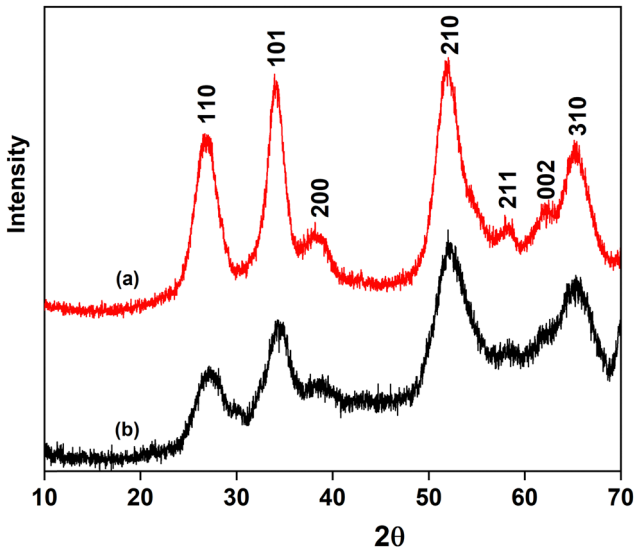

Fig. 1 XRD spectra of (a) SnO_2 NPs in a powder form and (b) SnO_2 NPs encapsulated within SA beads.

that rutile phase SnO_2 NPs are formed having broad peaks which indicates smaller particle size. Furthermore, Fig. 1(b) depicts that all the characteristic peaks for SnO_2 NPs are observed in the obtained XRD pattern for SnO_2@SA beads. Besides this, a similar pattern is observed for SnO_2@SA beads before and after adsorption as shown in ESI† (Fig. S3). The lowered intensities and the broadness of the peaks in the SnO_2@SA beads can be attributed to dispersion of SnO_2 NPs within the alginate polymer matrix.[41] No additional peak confirms the purity of the beads. Thus, the crystallinity and purity of SnO_2 NPs continue to be well-maintained after their successful encapsulation within SA beads. Similar observations have been reported by other studies based on encapsulation of nanoparticles within alginate beads.[42,43]

3.2 Optical Study

The structural properties of pure SnO_2 NPs were investigated using FTIR spectroscopic analysis. As shown in Fig. 2(a), the absorbance bands at 3348 cm^{-1} and 1621 cm^{-1} can be assigned to the hydroxyl group which may have resulted from the adsorbed water molecules on the surface of SnO_2 NPs.[44,45] The absorbance bands at 3348 cm^{-1} and the strong peak at 1621 cm^{-1} depict the stretching and bending mode of the OH groups, respectively.[45] Below the fingerprint region of the IR spectra, the characteristic features of the SnO_2 lattice can be highlighted by the presence of absorbance bands at 470 cm^{-1} which represent O–Sn–O stretching vibrations and the shoulder peaks at 639 cm^{-1}, collectively marking the stretching vibrations of Sn–O bonds.[16]

The analysis of SnO_2 NPs through Raman spectral data has been shown in Fig. 2(b). The spectrum of the synthesized SnO_2 shows bands at 120 cm^{-1}, 169 cm^{-1}, 301 cm^{-1}, 428 cm^{-1}, 567 cm^{-1}, 629 cm^{-1} and 774 cm^{-1}. The band found at 629 cm^{-1} represents the SnO_2 lattice structure, which is corroborated by the shoulder at 428 cm^{-1} reflecting the Sn–O–Sn linkage bending vibrations.[23]

 © 2023 The Author(s). Published by the Royal Society of Chemistry

Open Access Article. Published on 13 September 2023. Downloaded on 1/31/2026 1:12:25 PM.
This article is licensed under a Creative Commons Attribution-NonCommercial 3.0 Unported Licence.

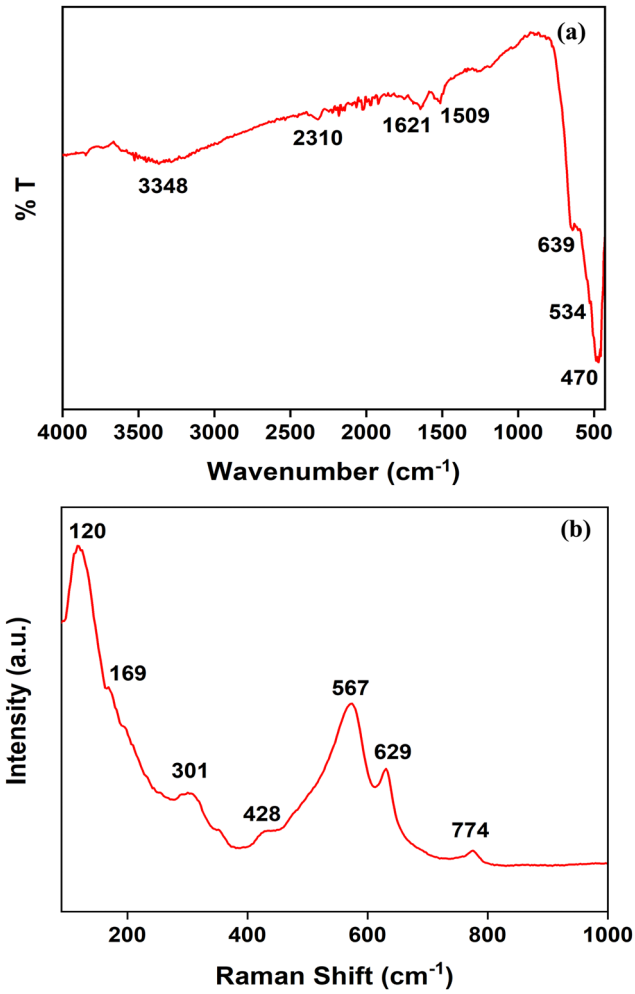

Fig. 2 (a) FTIR spectra and (b) Raman spectra of SnO_2 NPs.

Bridging and in-plane oxygen vacancies can be attributed to the bands at 567 cm^{-1} and 774 cm^{-1}, respectively.[16] Typically, a surface with oxygen vacancies exhibits high electron density, low adsorption energy, and rapid electron transfer.[46,47] The oxygen vacancies may aid in creating additional new active binding sites for adsorption.[48] Thus, the presence of oxygen vacancies on the synthesized nano-adsorbent can also be largely responsible for its high efficiency. Various similar studies have reported the presence of oxygen vacancies on metal oxides which lead to enhanced adsorption efficiency.[48–50]

3.3 Morphological study

The surface morphologies of SnO_2 NPs and SnO_2@SA beads were studied by scanning electron microscopy (SEM). Fig. 3(a) shows typical SEM images of the synthesized SnO_2 NPs. The morphologies clearly depict the formation of various sizes of spherical NPs (ESI,† Fig. S4a). Additionally, TEM images shown in Fig. 4(a) and (b) indicate the crystalline nature of NPs with a lattice fringe spacing of 3.36 Å which can be indexed to the (110) plane of SnO_2 NPs. It was observed that many lattice fringe spacings were within the approximate range of ≈3.34–3.63 Å. Also, elemental mapping of SnO_2 NPs for confirmation of elemental composition analysis has been obtained which

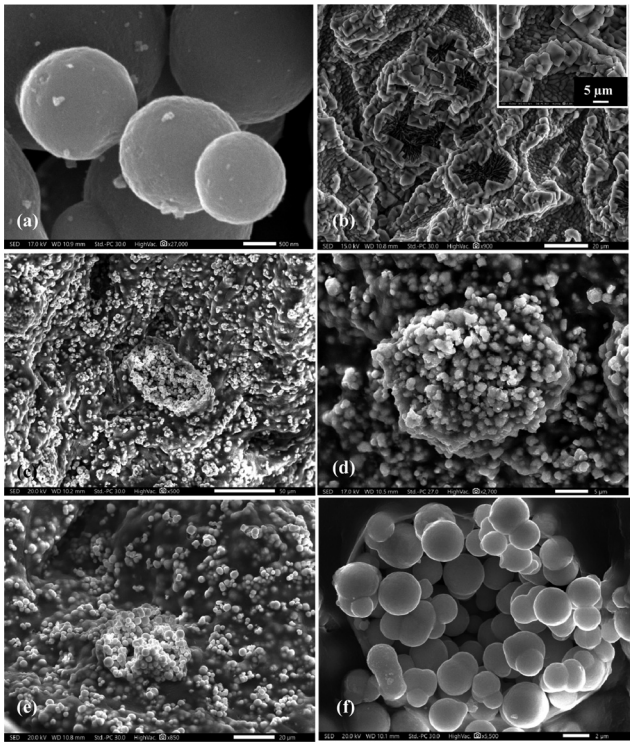

Fig. 3 SEM images of (a) SnO_2 NPs and (b) SA beads crosslinked by $CaCl_2$ at 20 µm, with the inset representing the image taken at 5 µm; panels (c), (d), (e) and (f) show 0.5 g SnO_2 encapsulated within SA beads at different magnification.

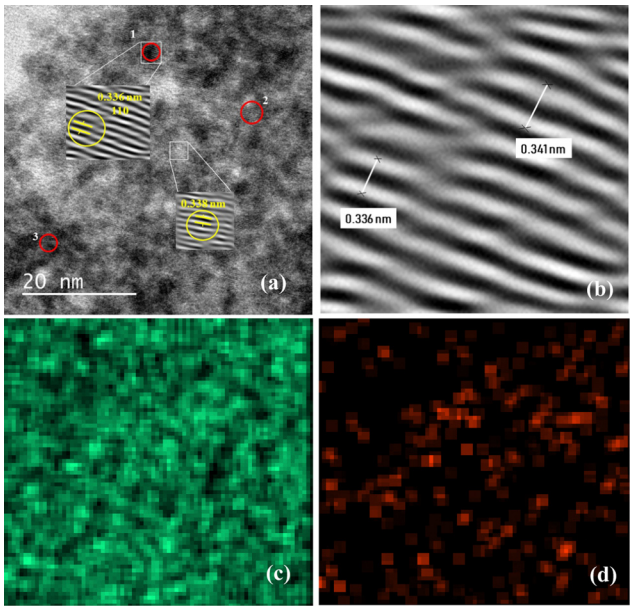

Fig. 4 (a) Enlarged view of TEM images of SnO_2 NPs showing various lattice fringes marked in a red circle; (b) magnified view of red circle 1 from image (a); and panels (c) and (d) show the elemental mapping of SnO_2 NPs with Sn and O in green and red colors, respectively.

Open Access Article. Published on 13 September 2023. Downloaded on 1/31/2026 1:12:25 PM.
This article is licensed under a Creative Commons Attribution-NonCommercial 3.0 Unported Licence.

confirmed SnO_2 NPs. The presence of each element has been highlighted, where the green color denotes the distribution of tin (Sn) and red denotes the distribution of oxygen (O) (Fig. 4(c) and (d)).

The morphological study of SnO_2@SA beads has also been carried out through SEM imaging. Fig. 3(b), with a higher magnification image in the inset, shows the surface morphology of completely dried pure SA beads, which clearly indicates long crosslinked chains. Upon encapsulation of 0.5 g SnO_2 within the SA beads, the surface morphology drastically changed as depicted in Fig. 3(c)–(f) which demonstrates that the spherically shaped SnO_2 NPs have been successfully entrapped within SA beads. Additionally, the SEM images for the encapsulation of 0.2 g SnO_2 within SA beads have been illustrated in ESI† (Fig. S4b–d) which clearly depict that at lower concentration (0.2 g SnO_2@SA beads, Fig. S4b–d, ESI†) the NPs are sparsely spread and entrapped, while at high concentration (0.5 g SnO_2@SA beads, Fig. 3(c)–(f)) the NPs are densely entrapped within SA beads.

4. Adsorption of anionic dyes

SnO_2 NPs were utilized as nano-adsorbents to remove four different anionic dyes (Congo red, eosin yellow, methyl orange, and orange G) from their aqueous solutions. In Fig. 5, the removal efficiency of SnO_2 NPs is depicted, revealing nearly complete removal (99.96%) of Congo red within 5 min of contact time. Moreover, the removal efficiency for eosin yellow after 30 min of contact time reaches approximately 82%. Additionally, 5.22% and 2.46% removal efficiencies are observed for orange G and methyl orange, respectively.

Adsorption studies were also conducted to evaluate the versatility of SnO_2@SA beads. The results, presented in Fig. 5(b), illustrate the adsorption capabilities of 0.3 g SnO_2@SA beads for eosin yellow, orange G, and methyl orange, in addition to Congo red. After a contact time of 30 min, the adsorption efficiencies were found to be 81%, 47.05%, 8.39%, and 5.53% for Congo red, eosin yellow, orange G, and methyl orange, respectively. This clearly demonstrates that SnO_2@SA beads possess the potential to effectively remove various anionic dyes, making them versatile candidates for wastewater treatment and environmental applications. The remarkable adsorption efficiency for Congo red and eosin yellow may also indicate the potential selectivity of the adsorbent for dyes with different molecular structure and charge densities. Besides, the moderate removal efficiencies for orange G and methyl orange indicate that SnO_2@SA beads can be further fine-tuned for specific dye removal applications. Based on the highest efficiency observed for Congo red dye, further investigations were carried out using Congo red to examine the influence of various operational parameters, as well as to study adsorption kinetics and isotherm.

5. Adsorption efficiency of SnO_2 nanoparticles

Various dye concentrations have been studied. The calibration curves and linear fit have been shown in ESI† (Fig. S5). The efficiency of adsorption by SnO_2 NPs is shown in Fig. 6(a). Within the first minute, fast adsorption of the dye occurs, resulting in more than 90% adsorption of the dye (Fig. S6a, ESI†). This high rate of adsorption may be credited to the large surface area of SnO_2 NPs, as confirmed through PXRD and SEM results. The removal efficiency (η) has been calculated using eqn (S1) discussed in the ESI† (S1).[17,51] The results revealed that nearly complete adsorption of organic pollutant CR has been successfully carried out within 5 min for the organic azo dye without the application of external factors such as cocatalyst, sacrificial agent, heat and light.

In the adsorption of organic dyes, a major role is played by the surface chemistry of the adsorbents. The favorable enhanced adsorption of CR dye by the synthesized NPs is to a great degree due to the electrostatic interaction between the cationic center of SnO_2 and the electron rich center of the CR dye.[52] Another major

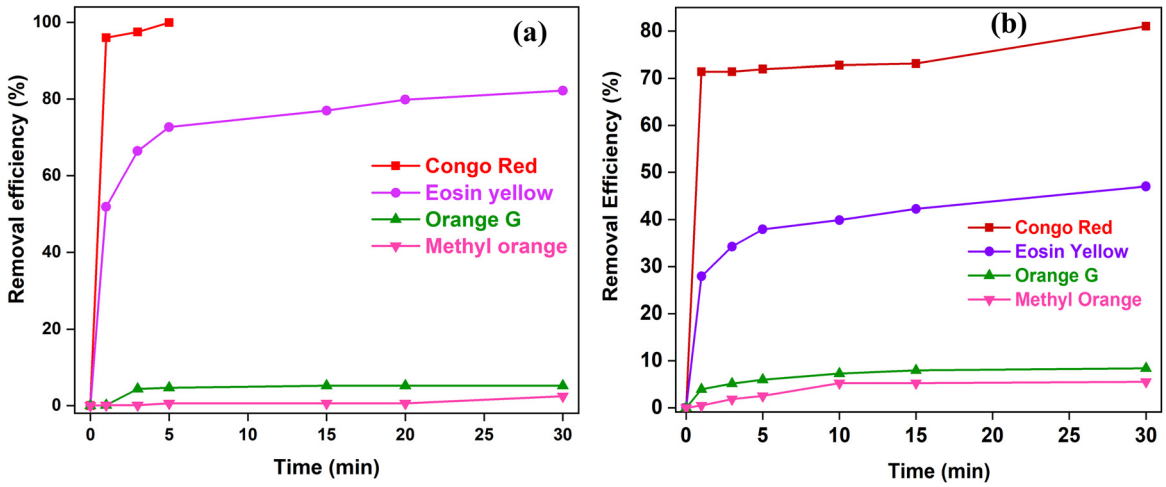

Fig. 5 Adsorption of four anionic dyes at a concentration of 5 μM using (a) 0.1 g/100 mL of SnO_2 NPs and (b) 0.3 g SnO_2@SA beads.

 © 2023 The Author(s). Published by the Royal Society of Chemistry

Open Access Article. Published on 13 September 2023. Downloaded on 1/31/2026 1:12:25 PM.
This article is licensed under a Creative Commons Attribution-NonCommercial 3.0 Unported Licence.

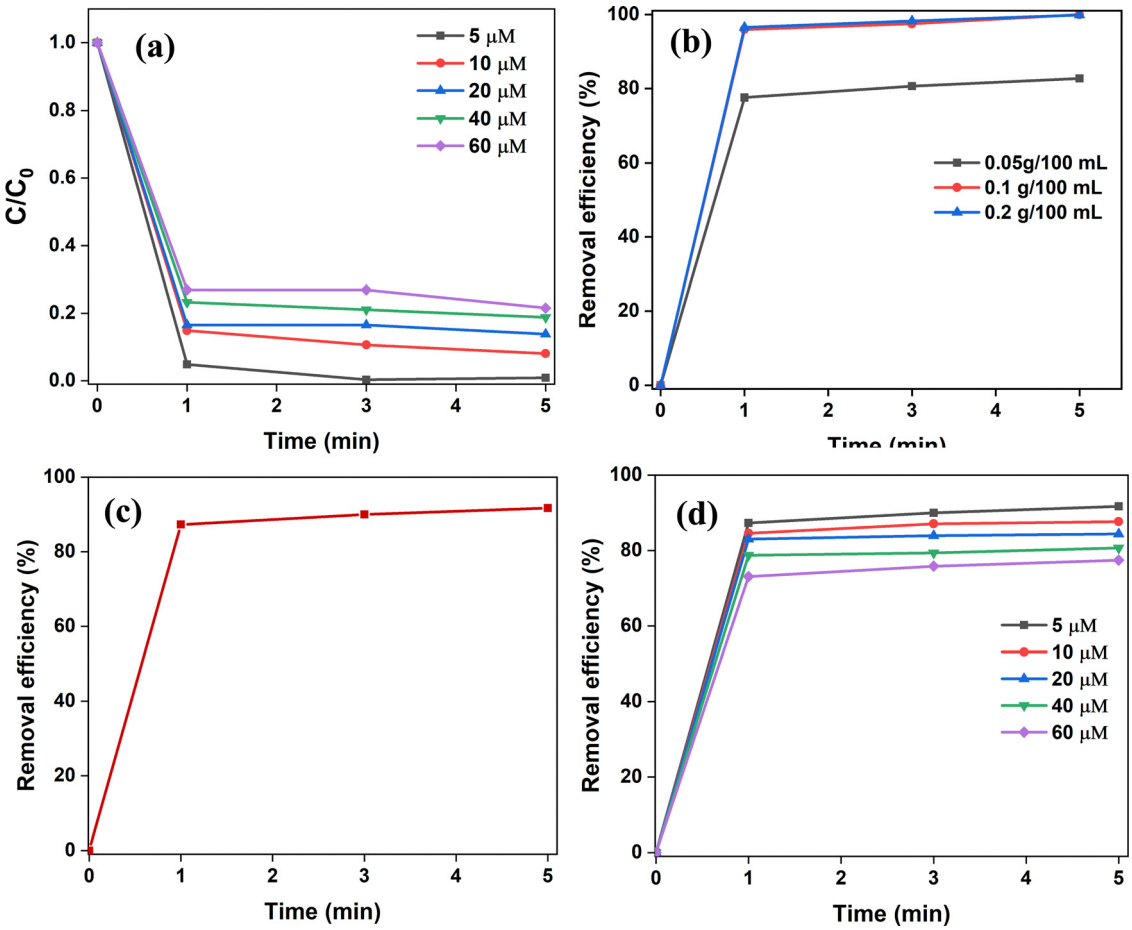

Fig. 6 (a) Adsorption efficiencies of spherical SnO_2 NPs as observed for various dye concentrations; (b) effect of adsorbent dosage on the removal efficiency for 5 μM CR at pH = 5; (c) effect of contact time upon the removal efficiency for 5 μM CR dye; and (d) effect of dye concentration on the removal efficiency for CR by 0.1 g/100 mL of SnO_2 NPs.

factor that can influence adsorption efficiency is the formation of oxygen vacancies. The presence of oxygen vacancies on the SnO_2 nano-adsorbent has been confirmed by Raman spectra, which are responsible for generating vacant active binding sites.[16,48,50] Also, additional capture of CR moieties may occur through the formation of hydrogen bonds.[53] This process is supported further by the fact that other reported positively charged adsorbents had significant adsorption capacity towards anionic dyes due to oxygen vacancies, electrostatic interactions and hydrogen bonding.[2,10,26,37,54,55]

5.1 Effect of adsorbent dose

At room temperature, the effect of adsorbent dosage has been investigated for 5 μM CR dye at different time intervals (0–5 min). The results are shown in Fig. 6(b), which indicates that increasing the adsorbent dose from 0.05 to 0.2 g/100 mL increases the percentage of adsorption for the entire contact time. This can be the consequence of increased surface area which further allows increased binding at active sites. The presence of additional adsorption active sites can also be responsible for the rise in adsorption effectiveness with the adsorbent dose.[56] However, at 5 min, the removal efficiencies of 0.1 and 0.2 g SnO_2 NPs are 99.96% and 99.83%, respectively. Since it does not indicate a significant difference, further investigations were carried out at 0.1 g/100 mL.

5.2 Effect of pH

pH is a significant parameter since it affects the adsorbent's surface charge, degree of ionization, and adsorbate speciation. Fig. 7 shows the influence of initial CR pH on the adsorption efficiency of SnO_2. The adsorbent dosage was kept fixed at 0.1 g/100 mL. At a varying pH range from 3 to 11, the predicted strong pH influence has been demonstrated for two dye concentrations (5 and 10 μM). At an initial pH of 5, maximum removal efficiency (~92%) for CR on SnO_2 was observed (Fig. 7(a)). However, at a pH lower than 5, as the acidic nature increased, its removal efficiency vastly declined to a much lower level. This can be due to the face-to-face arrangement of CR monomers into anionic dimers, which further allows them to partially self-associate and reduce their hydrophobic contact with water.[12] Thus, at highly acidic pH ranges (pH $<$ 5) CR dye may undergo tautomerism and aggregation, thereby hindering adsorption efficiency.[12] At pH $>$ 5, the increase in pH demonstrated a decline in the removal efficiency which can be due to interionic repulsions between similarly

Open Access Article. Published on 13 September 2023. Downloaded on 1/31/2026 1:12:25 PM.
This article is licensed under a Creative Commons Attribution-NonCommercial 3.0 Unported Licence.

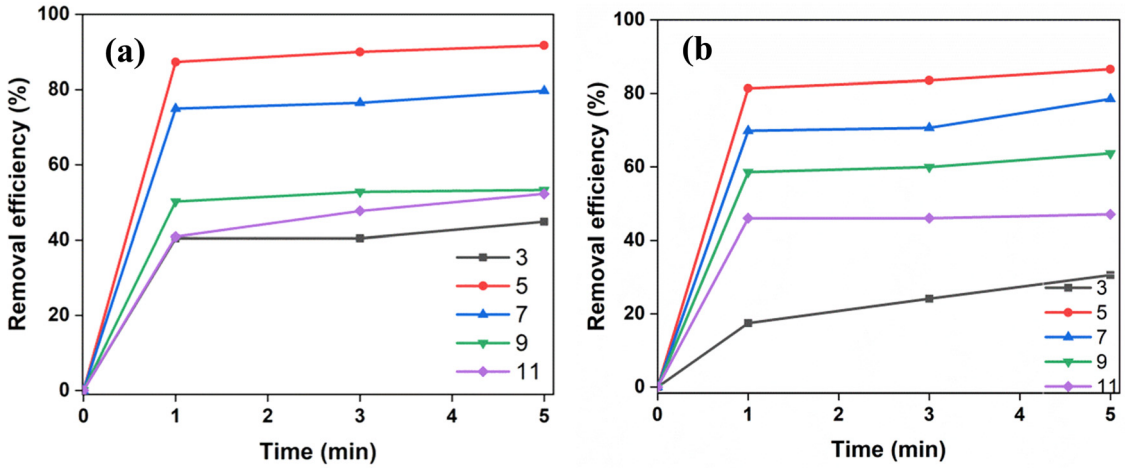

Fig. 7 Effect of pH on removal efficiency for two dye concentrations: (a) 5 μM and (b) 10 μM.

charged particles and the increased OH^- concentrations which compete for adsorption.[57,58] Therefore, the adsorption investigations were studied at an optimum pH = 5.

5.3 Effect of contact time

As illustrated in Fig. 6(c), the adsorption of CR on SnO_2 NPs was examined as a function of contact time to find the equilibrium for maximum adsorption. The adsorption rapidly increases within the 1st minute attaining more than 80% adsorption, after which it subsequently slows down as sorption equilibrium is attained after 5 min. Thus, it has been adopted as the optimum equilibrium time for the adsorption of CR dye on SnO_2 NP's surface at a CR concentration of 5 μM, pH = 5, and adsorbent dose of 0.1 g/100 mL. The rapid adsorption of CR within the first minute of contact depicts the large number of free active binding sites that are conveniently available for CR molecules.[17,51]

5.4 Effect of dye concentration

In adsorption, it is necessary to overcome the mass transfer resistance of the dye between the aqueous and solid phases.[59] This suggests that the initial concentration of the dye and its interaction with the adsorbent are crucial factors. In this context, the effect of initial dye concentration was studied for a range of 5–60 μM using a constant adsorbent dosage of 0.1 g/100 mL. Fig. 6(d) demonstrates that the increase of concentration from 5 to 60 μM resulted in a decreased percentage of dye removal efficiency. This is often related to the decrease in the number of vacant binding sites at high dye concentration, thereby lowering the adsorption driving force.[60]

6. Adsorption kinetics

The adsorption kinetics were determined at varying CR concentrations of 5–60 μM and at a fixed adsorbent dosage of 0.1 g/100 mL and pH = 5. For determining the appropriate model to describe the adsorption mechanism, the pseudo-first-order (PFO), pseudo-second-order (PSO) and intra-particle diffusion (IPD) models were applied (Fig. 8). The equations used for PFO, PSO and IPD have been discussed in the ESI† (S2).

The most appropriately fit model has been determined from comparative analysis based on the obtained linear regression correlation coefficient (R^2) values. The calculated kinetic parameters for each of the models have been summarized in Table 2. The results clearly depict that the PFO kinetics are not suitable for the present adsorption system due to the poor R^2 values. Additionally, the large difference between the experimental and calculated values of q_e demonstrated the poor fit of the PFO model. However, both PSO and IPD models demonstrated high R^2 values. However, R^2 values were more consistent and higher for PSO than for the IPD model. In addition to this, the calculated values of q_e for the PSO model are very well in agreement with the experimental q_e data. Secondly, the PSO kinetic model's curve-fitting plots demonstrated a straight line through the origin, validating it as the best fit model in the current system (Fig. 8(c)). This reflects that the adsorption mechanism involved in the adsorption of CR on SnO_2 NPs is facilitated by the process of chemisorption. This implies that the rate determining step is the chemical sorption of CR on the adsorbent's surface which may be simultaneously accompanied by exchange of electrons between adsorbate and adsorbent.[37]

7. Adsorption isotherm studies

In order to understand the interactive model between the adsorbent and the adsorbate, it is critical to evaluate adsorption isotherms since they provide unique insight into the nature of interactions. In this context, the renowned Langmuir, Freundlich and Temkin models were studied. The equations have been discussed in the ESI† (S3).

Fig. 9(a)–(c) depicts the CR adsorption isotherms of SnO_2 NPs for 5 μM CR at an adsorbent dosage of 0.1 g/100 mL having pH = 5. The R^2 value for the Langmuir isotherm is high (0.99988), while those for Freundlich and Temkin are 0.91772

 © 2023 The Author(s). Published by the Royal Society of Chemistry

Open Access Article. Published on 13 September 2023. Downloaded on 1/31/2026 1:12:25 PM.
This article is licensed under a Creative Commons Attribution-NonCommercial 3.0 Unported Licence.

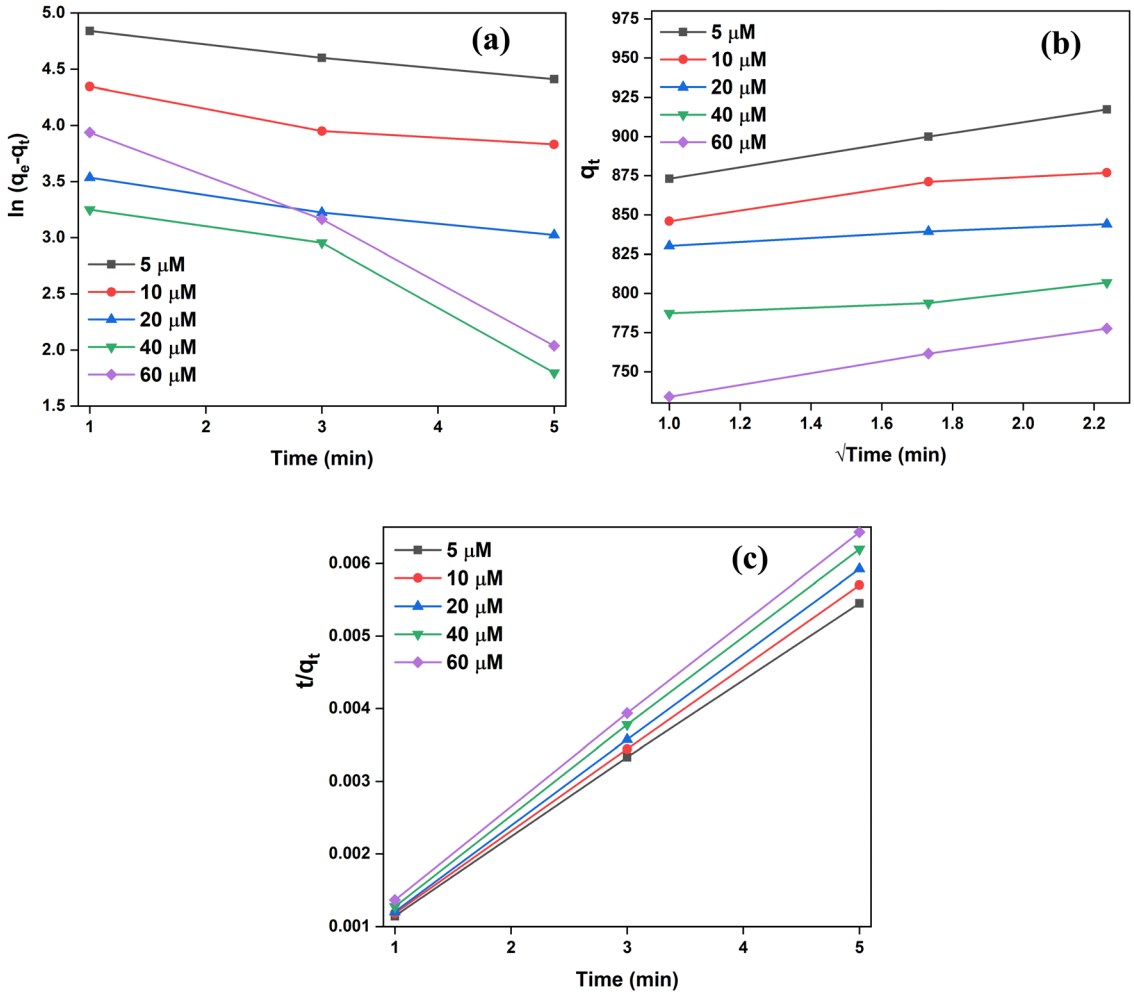

Fig. 8 Adsorption kinetic models studied for varying dye concentrations (5–60 μM) and a constant adsorbent dose (0.1 g/100 mL): (a) pseudo-first-order, (b) intra-particle diffusion and (c) pseudo-second-order.

Table 2 Kinetic parameters obtained from CR adsorption on SnO_2 NPs

Kinetic models	5 μM	10 μM	20 μM	40 μM	60 μM
$q_{e,exp}$ (mg g^{-1})	999.57	923.07	864.59	813.05	785.28
Pseudo-first-order					
R^2	0.9958	0.91193	0.99246	0.8948	0.98863
k_1 (min^{-1})	0.1057	0.1285	0.12824	0.3638	0.4749
$q_{e,cal}$ (mg g^{-1})	138.37	83.76	38.09	42.52	87.35
Pseudo-second-order					
R^2	0.99991	1	0.99999	0.99988	0.9999
k_2 (g mg^{-1} min^{-1})	0.0157	0.0246	0.0507	0.0283	0.0143
$q_{e,cal}$ (mg g^{-1})	929.925	884.95	847.45	813.00	793.65
Intra-particle diffusion					
R^2	0.99969	0.94341	0.99296	0.91478	0.99783
K_p (mg g^{-1} min$^{-1/2}$)	36.02	25.88	11.28	15.52	35.62

and 0.91787, respectively. The Langmuir isotherm model thus offered the most precise account of CR adsorption (Fig. 9(c)). Table S1 (ESI†) provides an overview of the three model's estimated parameters. The comparatively low R^2 values of Freundlich and Temkin isotherm models, however, led to their rejection. This suggests that CR was adsorbed at predetermined homogeneous sites of the nano-adsorbent, resulting in the formation of a monolayer on the nano-adsorbent's surface. Similar results have been reported in various other recent investigations related to dye adsorption, indicating that PSO and Langmuir isotherms are most commonly reported.[17,54,61–63] However, this does not eliminate the possibilities of adsorption kinetics and isotherms following other adsorption models.[64–66]

The favorability of the adsorption isotherm was further determined by evaluating the dimensionless separation factor (R_L), using eqn (S6) (ESI†).[67,68] The adsorption process favorability is determined by $0 < R_L < 1$.[10] It was determined that the value calculated for the adsorption of CR by the synthesized SnO_2 NPs lies within the range of 0 to 1 (R_L = 0.000113); thus the adsorption of CR on the adsorbent is determined to be favorable. Additionally, Table S1 (ESI†) compiles the information gathered from Freundlich isotherms, which clearly indicates that $1/n$ = 0.0083; hence the adsorption mechanism also fulfills the criteria for favorable reaction ($0 < 1/n < 1$).

Open Access Article. Published on 13 September 2023. Downloaded on 1/31/2026 1:12:25 PM.
This article is licensed under a Creative Commons Attribution-NonCommercial 3.0 Unported Licence.

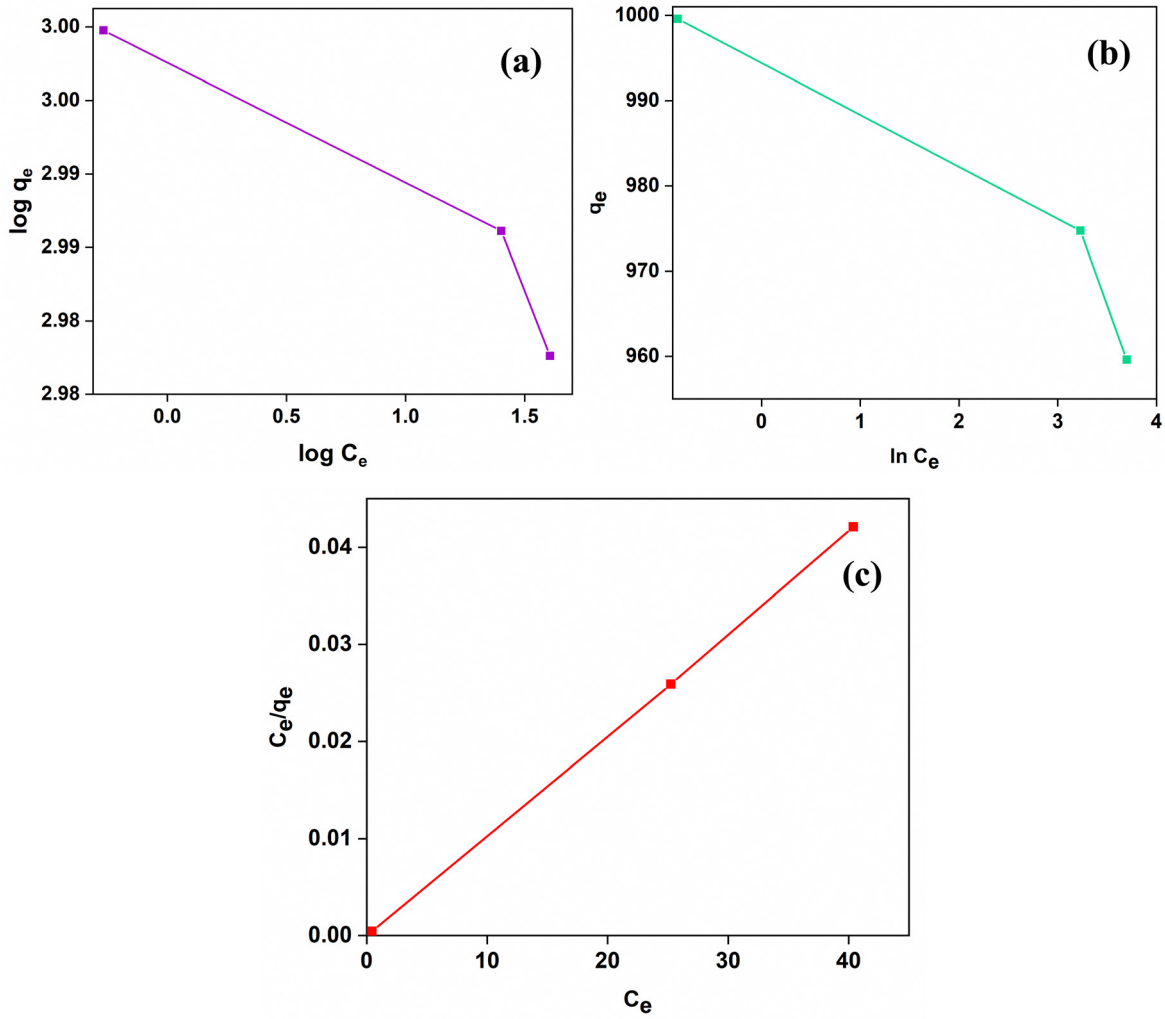

Fig. 9 Adsorption isotherms for 5 μM CR adsorption by SnO_2 at pH = 5 and room temperature. (a) Freundlich isotherm, (b) Temkin isotherm and (c) Langmuir isotherm.

8. Adsorption efficiency of encapsulated nanoparticles

Secondary pollutant generation due to metal leaching from the adsorbent and separation of the adsorbent from treated waters are two major challenges that need to be addressed for expanding the scope of pilot studies to practical implementation. To address these issues, SnO_2 NPs were encapsulated within sodium alginate (SnO_2@SA) beads. The adsorption efficiency of SnO_2@SA beads was evaluated for varying concentrations of SnO_2 (0.1 g, 0.2 g, and 0.5 g). However, to obtain a better comparative analysis, pure SA beads were first investigated for CR adsorption (Fig. 10(a)). For providing a clear perspective, the images of SnO_2 NPs and the completely dried SnO_2@SA beads are provided in the ESI† (Fig. S1). Additionally, Fig. S2 in the ESI† shows the images of the partially dried beads used for the adsorption studies. Fig. S1 (ESI†) illustrates the distinct color changes of the SnO_2 NPs and dried SnO_2@SA beads before and after adsorption. The white color of SnO_2 NPs changes to a pale red color, while similar changes in color are also observed for the dried SnO_2@SA beads. Thus, the adsorption of CR on both SnO_2 NPs and SnO_2@SA beads is quite evident through the color changes. Further analysis through UV-Visible spectroscopy has been carried out to clearly understand the comparative analysis of adsorption efficiency of SnO_2@SA beads of three different concentrations.

Pure SA beads demonstrated approximately 9% removal efficiency. Even after 10 min of exposure, the highest efficiency for pure SA beads is only about 25% (Fig. 10(a)). Upon encapsulating 0.1 g SnO_2 within SA beads (0.1 g SnO_2@SA beads), the efficiency increased to 32% within the first minute of contact. However, only 53% efficiency was attained after 10 min (Fig. S7, ESI†). Hence, 0.2 g and 0.5 g SnO_2@SA beads were also investigated. Increment in efficiency (63.82%) is typically observed for 0.2 g SnO_2@SA beads within 10 min (Fig. S8, ESI†), and nearly 75% efficiency is observed for 0.5 g SnO_2@SA beads within 5 min (Fig. S6b and S9, ESI†). Also, Fig. 10(b) depicts the comparative analysis of adsorption efficiencies of SnO_2 NPs and SnO_2@SA beads of various compositions in the form of a bar diagram. This indicates that the encapsulated SnO_2 NPs within SA beads can also show commendable efficiency when compared to SnO_2 NPs.

 © 2023 The Author(s). Published by the Royal Society of Chemistry

Open Access Article. Published on 13 September 2023. Downloaded on 1/31/2026 1:12:25 PM.
This article is licensed under a Creative Commons Attribution-NonCommercial 3.0 Unported Licence.

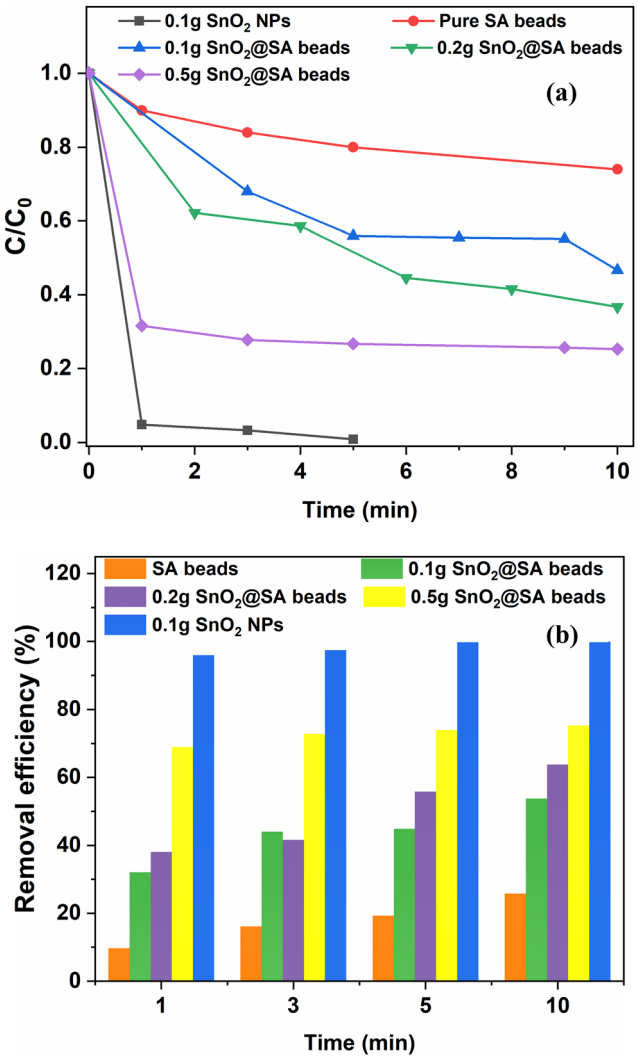

Fig. 10 (a) Various compositions of SnO_2@SA beads for CR dye adsorption, and (b) their comparative analysis through a bar diagram.

8.1. Leaching analysis

To ascertain leachate (Sn) concentrations in treated water, ICP-MS was employed to detect inorganic Sn within the treated water after utilizing 0.5 g SnO_2@SA beads, yielding a value of 7.729 ppb (parts per billion) or μg L^{-1}. This indicates that the Sn concentration in the treated water accounted for approximately 0.00019% of initial Sn concentration present in the beads (S4 in ESI†).

Assessments carried out by the WHO reported inorganic Sn concentration within the range of 0.2–3 μg L^{-1} in seawater, <0.003 μg L^{-1} in rainwater, and 0.001–8 μg L^{-1} in polluted coastal waters. Furthermore, UK drinking water supplies revealed Sn concentration to be below 10 μg L^{-1}, while an average concentration of 6 μg L^{-1} was reported in US municipal drinking water.[69] The Joint FAO/WHO expert committee on Food Additives also reported that the maximum level of Sn in commodities such as canned food and beverages must not exceed 250 mg kg^{-1} and 150 mg kg^{-1}, respectively.[70] They also concluded that Sn concentration higher than 200 ppm can produce acute toxic effects in humans. Similarly, a study based in Perak, Malaysia, reported Sn concentration ranging between 1 and 7 μg L^{-1}.[71] More recently, the WHO released the 4th edition incorporating guidelines for drinking-water quality, which revealed that considering the minimal toxicity of reported Sn concentration, the establishment of permissible levels for Sn has been deemed unnecessary.[72] Consequently, the direct comparison of measured Sn concentrations in treated water using SnO_2@SA beads based on existing literature is not feasible. Nonetheless, it can be surmised that the detected Sn concentration identified in this work remains lower in comparison to the benchmarks reported in the existing literature. Thus, the pragmatic application of these beads as nano-adsorbents exhibits significant potential for treating dye wastewater. However, scaling up of these nanosorbents requires further in-depth exploration which will be performed to ensure complete mitigation of Sn leaching in treated water.

9. Regenerative studies

The stability of an adsorbent plays a crucial role when it undergoes repeated adsorption–desorption cycles. To establish the reusability, feasibility and cost-effectiveness of SnO_2@SA beads were assessed through chemical regeneration using solvent desorption. This method of regeneration has substantial advantages as it has an environmentally benign nature, low-cost, and rapid regeneration rate. Fig. 11 presents comparative desorption efficiencies of acetone, methanol, ethanol and dil. HCl. Acetone and methanol exhibited the highest desorption efficiency, surpassing ethanol and dil. HCl significantly. However, considering the highly volatile nature of acetone, which may lead to incomplete desorption due to rapid evaporation, methanol was selected as the preferred eluent for further regeneration studies.

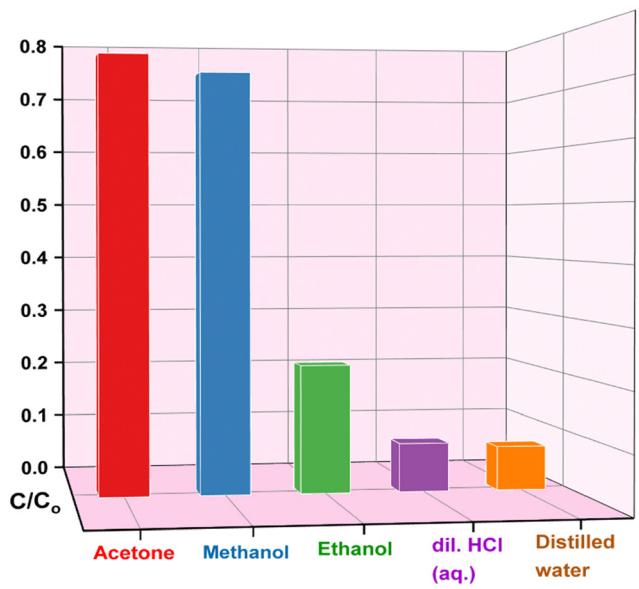

Fig. 11 Bar diagram showing the concentration of desorbed Congo red in various eluents from the adsorbent.

Open Access Article. Published on 13 September 2023. Downloaded on 1/31/2026 1:12:25 PM.
This article is licensed under a Creative Commons Attribution-NonCommercial 3.0 Unported Licence.

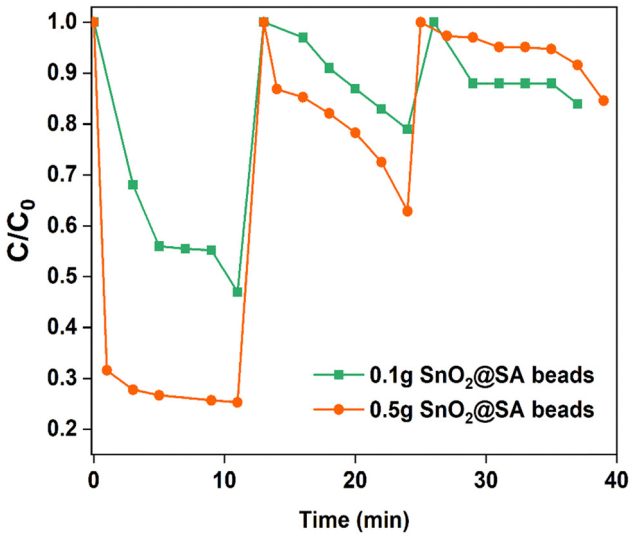

Fig. 12 Regenerative studies of 0.5 g and 0.1 g SnO_2@SA beads for 5 μM CR aqueous solution.

SnO_2@SA beads were used to perform three consecutive cycles using methanol as an eluent (Fig. S10, ESI†) and the results are shown in Fig. 12. The amount of CR adsorption gradually decreases as the number of cycles increases. The amount of adsorbed dye that was not recovered by desorption was likely present on the beads, which caused a gradual reduction in adsorption capacity in the following cycles.[6] The lowered efficiency may be attributed to the unavailable or attenuated vacant adsorption sites during desorption.[35] The CR adsorption capacity of 0.5 g SnO_2@SA beads decreased from 75.3% to 18.9% after two cycles, while that of 0.1 g SnO_2@SA beads decreased from 53.7% to 15.1% after two cycles (Fig. 12). As a result, it can be inferred that SnO_2@SA beads are promising environmentally friendly nano-adsorbents for treatment of CR dye. However, more investigation is required to identify the ideal eluent to boost the efficacy of the reusability of SnO_2@SA beads.

10. Comparison with other adsorbents

Various adsorbents such as activated carbon obtained from agricultural waste biomass,[73] walnut shell[74] and carboxymethyl cellulose,[75] metal organic frameworks like UiO-66[13] and even starch based hydrogels[76] have been fabricated for the adsorption of CR and many other dyes such as methylene blue. The comparison of the presented work using SnO_2 NPs with other adsorbents used for the treatment of CR dye is shown in Table 3. It clearly indicates that the maximum adsorption capacity of SnO_2 NPs is quite high and even better than that of some of the reported studies. Abdelkader *et al.* reported 84.41% Congo red removal efficiency after 60 min of contact time using SnO_2 NPs which were synthesized at 450 and 650 °C.[17] In contrast, the current study achieved significantly higher efficiency, demonstrated regenerative abilities, and showcased versatility in adsorbing multiple anionic dyes by SnO_2 NPs synthesized at a comparatively low temperature, even when encapsulated within sodium alginate beads. Therefore, these nano-adsorbents can be considered as of great potential for the treatment of anionic dyes. Moreover, the successful implementation of SnO_2 NPs encapsulated within SA beads can provide immense control over the leaching of metal from the nano-adsorbent, thereby proving them to be a biocompatible, highly efficient and economical adsorbent.

11. Conclusion

In this study, hydrothermally synthesized spherical SnO_2 NPs were successfully prepared without any toxic reagents. PXRD, TEM, FTIR and Raman spectroscopy confirmed the formation of SnO_2 NPs. SEM imaging confirmed the formation of spherical NPs and the encapsulation of SnO_2 NPs in sodium alginate beads. Within 1 min, nearly 95% adsorption efficiency is observed for 5 μM CR dye by 0.1 g/100 mL of SnO_2 NPs. Favorable adsorption is determined to be at pH = 5, while adsorption decreases at highly acidic and basic pH. The adsorption behavior can be best described by pseudo-second-order kinetics. The equilibrium data displayed the best fit of the Langmuir isotherm and the maximum adsorption capacity was determined to be 961.5 mg g^{-1}. The driving forces can be attributed to oxygen vacancies, electrostatic force of attraction and hydrogen bonding, and the adsorption mechanism involved chemisorption and monolayer formation on adsorbent's surface. Finally, the encapsulated SnO_2 NPs within sodium alginate beads were also capable of behaving as nano-adsorbents for CR dye removal, which also showed

Table 3 Comparison of various adsorbents used for removal of CR dye

Adsorbent	Adsorbent dosage	Adsorption capacity, q_m (mg g^{-1})	Isotherm	Kinetic model	Ref.
$Cd_4(H_4L)_2(phen)_2(H_2O)_4$	3000 g mL^{-1}	684	Langmuir	Pseudo-second order	77
Activated carbon from water hyacinth stem	16 g L^{-1}	14.367	Langmuir	Pseudo-second order	78
Cyanoguanidine-modified chitosan	50 mg/50 mL	666.67	Langmuir	Pseudo-second order	79
AlF-rGO	0.1 g/25 mL	178.57	Freundlich	Pseudo-second order	80
Vernonia amygdalina leaf powder	5 g L^{-1}	57.47	Langmuir	Pseudo-second order	81
Fe_3O_4/graphene oxide composite	—	769.2	Langmuir	Pseudo-second order	67
$CoFe_{2-x}Gd_xO_4$	—	263.2	Langmuir	Pseudo-second order	82
Fe_3O_4@SiO_2-COOH NPs	0.5 g L^{-1}	263.16	Langmuir	Pseudo-second order	51
SnO_2 NPs	1 g L^{-1}	48.31	Langmuir	Pseudo-second order	17
SnO_2 NPs	0.1 g/100 mL	961.54	Langmuir	Pseudo-second order	This work

 © 2023 The Author(s). Published by the Royal Society of Chemistry

Open Access Article. Published on 13 September 2023. Downloaded on 1/31/2026 1:12:25 PM.
This article is licensed under a Creative Commons Attribution-NonCommercial 3.0 Unported Licence.

successful regeneration. Additionally, nearly 0.0019% of Sn concentration from the adsorbent material was detected in aqueous solution after treating dyes, which indicates significantly reduced metal leaching due to encapsulation of SnO_2 in alginate beads. Moreover, the noteworthy adsorption capabilities of SnO_2@SA beads extend beyond Congo red dye, as they also demonstrate adsorption of eosin yellow, orange G and methyl orange. In conclusion, SnO_2@SA beads have high potential in dye wastewater treatment due to their ease of preparation, environmental friendliness, and cost-effectiveness. Nevertheless, efforts to improve the effectiveness of SnO_2@SA beads through doping or the production of nanocomposites can be pursued in future studies.

Declaration of generative AI in scientific writing

Not applicable.

Conflicts of interest

The authors declare that they have no conflict of interest.

Acknowledgements

The author S. J. B is grateful to Jawaharlal Nehru University, New Delhi, for providing financial assistance. This research did not receive any specific grant from funding agencies in the public, commercial, or not-for-profit sectors.

References

1 E. J. R. Almeida and C. R. Corso, Decolorization and removal of toxicity of textile azo dyes using fungal biomass pelletized, *Int. J. Environ. Sci. Technol.*, 2019, **16**, 1319–1328.
2 Y. Zheng, B. Cheng, J. Fan, J. Yu and W. Ho, Review on nickel-based adsorption materials for Congo red, *J. Hazard. Mater.*, 2021, **403**, 123559.
3 T. N. J. I. Edison, R. Atchudan, M. G. Sethuraman and Y. R. Lee, Reductive-degradation of carcinogenic azo dyes using Anacardium occidentale testa derived silver nanoparticles, *J. Photochem. Photobiol., B*, 2016, **162**, 604–610.
4 R. G. Saratale, G. D. Saratale, J.-S. Chang and S. P. Govindwar, Bacterial decolorization and degradation of azo dyes: a review, *J. Taiwan Inst. Chem. Eng.*, 2011, **42**, 138–157.
5 S.-S. Yang, J.-H. Kang, T.-R. Xie, L. He, D.-F. Xing, N.-Q. Ren, S.-H. Ho and W.-M. Wu, Generation of high-efficient biochar for dye adsorption using frass of yellow mealworms (larvae of Tenebrio molitor Linnaeus) fed with wheat straw for insect biomass production, *J. Cleaner Prod.*, 2019, **227**, 33–47.
6 V. S. Munagapati and D.-S. Kim, Equilibrium isotherms, kinetics, and thermodynamics studies for congo red adsorption using calcium alginate beads impregnated with nano-goethite, *Ecotoxicol. Environ. Saf.*, 2017, **141**, 226–234.
7 R. K. Sonwani, G. Swain, B. S. Giri, R. S. Singh and B. N. Rai, Biodegradation of Congo red dye in a moving bed biofilm reactor: Performance evaluation and kinetic modeling, *Bioresour. Technol.*, 2020, **302**, 122811.
8 S. Chakraborty, J. J. Farida, R. Simon, S. Kasthuri and N. L. Mary, Averrhoe carrambola fruit extract assisted green synthesis of zno nanoparticles for the photodegradation of congo red dye, *Surf. Interfaces*, 2020, **19**, 100488.
9 N. P. Khumalo, L. N. Nthunya, E. De Canck, S. Derese, A. R. Verliefde, A. T. Kuvarega, B. B. Mamba, S. D. Mhlanga and D. S. Dlamini, Congo red dye removal by direct membrane distillation using PVDF/PTFE membrane, *Sep. Purif. Technol.*, 2019, **211**, 578–586.
10 J. Liu, N. Wang, H. Zhang and J. Baeyens, Adsorption of Congo red dye on $Fe_xCo_{3-x}O_4$ nanoparticles, *J. Environ. Manage.*, 2019, **238**, 473–483.
11 S. Yu, J. Wang and J. Cui, Preparation of a novel chitosan-based magnetic adsorbent CTS@ SnO_2@Fe_3O_4 for effective treatment of dye wastewater, *Int. J. Biol. Macromol.*, 2020, **156**, 1474–1482.
12 Z. L. Yaneva and N. V. Georgieva, Insights into Congo Red Adsorption on Agro-Industrial Materials-Spectral, Equilibrium, Kinetic, Thermodynamic, Dynamic and Desorption Studies. A Review, *Int. Rev. Chem. Eng.*, 2012, **4**, 127–146.
13 F. Ahmadijokani, R. Mohammadkhani, S. Ahmadipouya, A. Shokrgozar, M. Rezakazemi, H. Molavi, T. M. Aminabhavi and M. Arjmand, Superior chemical stability of UiO-66 metal-organic frameworks (MOFs) for selective dye adsorption, *Chem. Eng. J.*, 2020, **399**, 125346.
14 Q. Du, J. Sun, Y. Li, X. Yang, X. Wang, Z. Wang and L. Xia, Highly enhanced adsorption of congo red onto graphene oxide/chitosan fibers by wet-chemical etching off silica nanoparticles, *Chem. Eng. J.*, 2014, **245**, 99–106.
15 Bhawna, S. Kumar, R. Sharma, A. Gupta, A. Tyagi, P. Singh, A. Kumar and V. Kumar, Recent insights into SnO_2-based engineered nanoparticles for sustainable H_2 generation and remediation of pesticides, *New J. Chem.*, 2022, **46**, 4014–4048.
16 S. Kumar, Bhawna, S. K. Yadav, A. Gupta, R. Kumar, J. Ahmed, M. Chaudhary, Suhas and V. Kumar, B-doped SnO_2 nanoparticles: a new insight into the photocatalytic hydrogen generation by water splitting and degradation of dyes, *Environ. Sci. Pollut. Res.*, 2022, **29**, 47448–47461.
17 E. Abdelkader, L. Nadjia and V. Rose-Noëlle, Adsorption of Congo red azo dye on nanosized SnO_2 derived from sol–gel method, *Int. J. Ind. Chem.*, 2016, **7**, 53–70.
18 H.-C. Chiu and C.-S. Yeh, Hydrothermal synthesis of SnO_2 nanoparticles and their gas-sensing of alcohol, *J. Phys. Chem. C*, 2007, **111**, 7256–7259.
19 G. X. Wang, Y. Chen, L. Yang, J. Yao, S. Needham, H. K. Liu and J. H. Ahn, Synthesis of nanocrystalline transition metal and oxides for lithium storage, *J. Power Sources*, 2005, **146**, 487–491.
20 N. Talebian and H. S. H. Zavvare, Enhanced bactericidal action of SnO_2 nanostructures having different morphologies under

Open Access Article. Published on 13 September 2023. Downloaded on 1/31/2026 1:12:25 PM.
This article is licensed under a Creative Commons Attribution-NonCommercial 3.0 Unported Licence.

visible light: influence of surfactant, *J. Photochem. Photobiol., B*, 2014, **130**, 132–139.
21 G. Korotcenkov, *Nanomaterials*, 2020, **10**, 1392.
22 P. G. Jamkhande, N. W. Ghule, A. H. Bamer and M. G. Kalaskar, Metal nanoparticles synthesis: An overview on methods of preparation, advantages and disadvantages, and applications, *J. Drug Delivery Sci. Technol.*, 2019, **53**, 101174.
23 V. Kumar, K. Yadav, A. Gupta and B. Dwivedi, Facile Synthesis of Ce – Doped SnO_2 Nanoparticles: A Promising Photocatalyst for Hydrogen Evolution and Dyes Degradation, *ChemistrySelect*, 2019, 3722–3729.
24 Y. Wang, X. Jiang and Y. Xia, A solution-phase, precursor route to polycrystalline SnO_2 nanowires that can be used for gas sensing under ambient conditions, *J. Am. Chem. Soc.*, 2003, **125**, 16176–16177.
25 V. Kumar and R. Nagarajan, Thermoluminescence in heavily F-doped of SnO_2 nanocrystals, *Chem. Phys. Lett.*, 2012, **530**, 98–101.
26 J. P. Dhal, B. G. Mishra and G. Hota, Fe_2O_3–SnO_2 composite nanorods: Facile synthesis and sorption properties, *J. Environ. Chem. Eng.*, 2014, **2**, 2188–2198.
27 A. F. Beevi, G. Sreekala and B. Beena, Synthesis, characterization and photocatalytic activity of SnO_2, ZnO nanoparticles against congo red: A comparative study, *Mater. Today: Proc.*, 2021, **45**, 4045–4051.
28 X. Chen, F. Zhang, Q. Wang, X. Han, X. Li, J. Liu, H. Lin and F. Qu, The synthesis of ZnO/SnO_2 porous nanofibers for dye adsorption and degradation, *Dalton Trans.*, 2015, **44**, 3034–3042.
29 C. M. Ma, G. B. Hong and S. C. Lee, *Catalysts*, 2020, 10.
30 M. Maruthupandy, T. Muneeswaran, G. Chackaravarthi, T. Vennila, M. Anand, W.-S. Cho and F. Quero, Synthesis of chitosan/SnO_2 nanocomposites by chemical precipitation for enhanced visible light photocatalytic degradation efficiency of congo red and rhodamine-B dye molecules, *J. Photochem. Photobiol., A*, 2022, **430**, 113972.
31 D. Zhao and X. Wu, Nanoparticles assembled SnO_2 nanosheet photocatalysts for wastewater purification, *Mater. Lett.*, 2018, **210**, 354–357.
32 V. Rocher, A. Bee, J.-M. Siaugue and V. Cabuil, Dye removal from aqueous solution by magnetic alginate beads crosslinked with epichlorohydrin, *J. Hazard. Mater.*, 2010, **178**, 434–439.
33 M. A. El-Bindary, I. M. El-Deen and A. F. Shoair, Removal of anionic dye from aqueous solution using magnetic sodium alginate beads, *J. Mater. Environ. Sci.*, 2019, **10**, 604–617.
34 E. Tao, D. Ma, S. Yang and X. Hao, Graphene oxide-montmorillonite/sodium alginate aerogel beads for selective adsorption of methylene blue in wastewater, *J. Alloys Compd.*, 2020, **832**, 154833.
35 X. Zhao, X. Wang and T. Lou, Preparation of fibrous chitosan/sodium alginate composite foams for the adsorption of cationic and anionic dyes, *J. Hazard. Mater.*, 2021, **403**, 124054.
36 H. Rezaei, M. Haghshenasfard and A. Moheb, Optimization of dye adsorption using Fe_3O_4 nanoparticles encapsulated with alginate beads by Taguchi method, *Adsorpt. Sci. Technol.*, 2017, **35**, 55–71.
37 Y. Feng, H. Wang, J. Xu, X. Du, X. Cheng, Z. Du and H. Wang, Fabrication of MXene/PEI functionalized sodium alginate aerogel and its excellent adsorption behavior for Cr(VI) and Congo Red from aqueous solution, *J. Hazard. Mater.*, 2021, **416**, 125777.
38 M. E. González-López, C. M. Laureano-Anzaldo, A. A. Pérez-Fonseca, C. Gómez and J. R. Robledo-Ortíz, Congo red adsorption with cellulose-graphene nanoplatelets beads by differential column batch reactor, *J. Environ. Chem. Eng.*, 2021, **9**, 105029.
39 H. S. Hassan, M. F. Elkady, A. H. El-Shazly and H. S. Bamufleh, Formulation of synthesized zinc oxide nanopowder into hybrid beads for dye separation, *J. Nanomater.*, 2014, **2014**, 6.
40 S. Yadav, A. Asthana, A. K. Singh, R. Chakraborty, S. Sree Vidya, A. Singh and S. A. C. Carabineiro, Methionine-functionalized graphene oxide/sodium alginate biopolymer nanocomposite hydrogel beads: synthesis, isotherm and kinetic studies for an adsorptive removal of fluoroquinolone antibiotics, *Nanomaterials*, 2021, **11**, 568.
41 M. Amiri, M. Salavati-Niasari, A. Pardakhty, M. Ahmadi and A. Akbari, Caffeine: A novel green precursor for synthesis of magnetic $CoFe_2O_4$ nanoparticles and pH-sensitive magnetic alginate beads for drug delivery, *Mater. Sci. Eng., C*, 2017, **76**, 1085–1093.
42 X. Yi, J. He, Y. Guo, Z. Han, M. Yang, J. Jin, J. Gu, M. Ou and X. Xu, Encapsulating Fe_3O_4 into calcium alginate coated chitosan hydrochloride hydrogel beads for removal of Cu(II) and U(VI) from aqueous solutions, *Ecotoxicol. Environ. Saf.*, 2018, **147**, 699–707.
43 S. Periyasamy, V. Gopalakannan and N. Viswanathan, Hydrothermal assisted magnetic nano-hydroxyapatite encapsulated alginate beads for efficient Cr(VI) uptake from water, *J. Environ. Chem. Eng.*, 2018, **6**, 1443–1454.
44 F. Gu, S. F. Wang, C. F. Song, M. K. Lü, Y. X. Qi, G. J. Zhou, D. Xu and D. R. Yuan, Synthesis and luminescence properties of SnO_2 nanoparticles, *Chem. Phys. Lett.*, 2003, **372**, 451–454.
45 R. Scipioni, D. Gazzoli, F. Teocoli, O. Palumbo, A. Paolone, N. Ibris, S. Brutti and M. A. Navarra, *Membranes*, 2014, **4**, 123–142.
46 N. Zhang, E. P. Tsang, J. Chen, Z. Fang and D. Zhao, Critical role of oxygen vacancies in heterogeneous Fenton oxidation over ceria-based catalysts, *J. Colloid Interface Sci.*, 2020, **558**, 163–172.
47 J. Liu, O. Margeat, W. Dachraoui, X. Liu, M. Fahlman and J. Ackermann, Gram-scale synthesis of ultrathin tungsten oxide nanowires and their aspect ratio-dependent photocatalytic activity, *Adv. Funct. Mater.*, 2014, **24**, 6029–6037.
48 N. Cao, X. Zhao, M. Gao, Z. Li, X. Ding, C. Li, K. Liu, X. Du, W. Li, J. Feng, Y. Ren and T. Wei, Superior selective adsorption of MgO with abundant oxygen vacancies to removal and recycle reactive dyes, *Sep. Purif. Technol.*, 2021, **275**, 119236.

 © 2023 The Author(s). Published by the Royal Society of Chemistry

Open Access Article. Published on 13 September 2023. Downloaded on 1/31/2026 1:12:25 PM.
This article is licensed under a Creative Commons Attribution-NonCommercial 3.0 Unported Licence.

49 Y.-F. Sun, J.-J. Li, F. Xie, Y. Wei and M. Yang, Ruthenium-loaded cerium dioxide nanocomposites with rich oxygen vacancies promoted the highly sensitive electrochemical detection of Hg(II), *Sens. Actuators, B*, 2020, **320**, 128355.
50 P. Ren, X. Ren, J. Xu, H. Li, Y. Zheng, Y. Hong, Y. Lin, Y. Zhou, Y. Chen and W. Zhang, Excellent adsorption property and mechanism of oxygen vacancies-assisted hexagonal MoO_3 nanosheets for methylene blue and rhodamine b dyes, *Appl. Surf. Sci.*, 2022, **597**, 153699.
51 M. Mohammadi Galangash, M. Mohaghegh Montazeri, A. Ghavidast and M. Shirzad-Siboni, Synthesis of carboxyl-functionalized magnetic nanoparticles for adsorption of malachite green from water: Kinetics and thermodynamics studies, *J. Chin. Chem. Soc.*, 2018, **65**, 940–950.
52 G. Sangami and N. Dharmaraj, UV-visible spectroscopic estimation of photodegradation of rhodamine-B dye using tin(IV) oxide nanoparticles, *Spectrochim. Acta, Part A*, 2012, **97**, 847–852.
53 X. Liu, Z. Zhang, W. Shi, Y. Zhang, S. An and L. Zhang, Adsorbing properties of magnetic nanoparticles Mn-ferrites on removal of Congo red from aqueous solution, *J. Dispersion Sci. Technol.*, 2015, **36**, 462–470.
54 M. P. Rao, A. K. Akhila, J. J. Wu, A. M. Asiri and S. Anandan, Synthesis, characterization and adsorption properties of $Cu_2V_2O_7$ nanoparticles, *Solid State Sci.*, 2019, **92**, 13–23.
55 T. Mahmood, U. Noreen, R. Ali, A. Ullah, A. Naeem and M. Aslam, Adsorptive removal of Congo red from aqueous phase using graphene–tin oxide composite as a novel adsorbent, *Int. J. Environ. Sci. Technol.*, 2022, **19**, 10275–10290.
56 J.-S. Cao, J.-X. Lin, F. Fang, M.-T. Zhang and Z.-R. Hu, A new absorbent by modifying walnut shell for the removal of anionic dye: kinetic and thermodynamic studies, *Bioresour. Technol.*, 2014, **163**, 199–205.
57 R. Sivaraj, C. Namasivayam and K. Kadirvelu, Orange peel as an adsorbent in the removal of acid violet 17 (acid dye) from aqueous solutions, *Waste Manag.*, 2001, **21**, 105–110.
58 S. Mishra, D. J. Prakash and G. Ramakrishna, Characterization and utilization of mahua oil cake–A new adsorbent for the removal of congored dye from aqueous phase, *Electron. J. Environ., Agric. Food Chem.*, 2009, **8**, 425–436.
59 Y. Önal, C. Akmil-Başar and Ç. Sarıcı-Özdemir, Investigation kinetics mechanisms of adsorption malachite green onto activated carbon, *J. Hazard. Mater.*, 2007, **146**, 194–203.
60 M. Bhaumik, T. Y. Leswifi, A. Maity, V. V. Srinivasu and M. S. Onyango, Removal of fluoride from aqueous solution by polypyrrole/Fe_3O_4 magnetic nanocomposite, *J. Hazard. Mater.*, 2011, **186**, 150–159.
61 Y. Tang, X. Zhang, X. Li, J. Bai, C. Yang, Y. Zhang, Z. Xu, X. Jin and Y. Jiang, Facile synthesis of magnetic ZnAl layered double hydroxides and efficient adsorption of malachite green and Congo red, *Sep. Purif. Technol.*, 2023, **322**, 124305.
62 N. Ahmad, F. Suryani Arsyad, I. Royani, P. Mega Syah Bahar Nur Siregar, T. Taher and A. Lesbani, High regeneration of ZnAl/NiAl-Magnetite humic acid for adsorption of Congo red from aqueous solution, *Inorg. Chem. Commun.*, 2023, **150**, 110517.
63 M. T. Moustafa, Preparation and characterization of low-cost adsorbents for the efficient removal of malachite green using response surface modeling and reusability studies, *Sci. Rep.*, 2023, **13**, 4493.
64 R. El yousfi, N. Achalhi, A. Mohamed, A. Benahmed and A. El Idrissi, Synthesis, characterization of multi-arm copolymers and linear blocks based on PEG and PCL: Effect of topology on dye adsorption, *Mater. Today: Proc.*, 2023, **72**, 3650–3661.
65 P. K. Rose, R. Kumar, R. Kumar, M. Kumar and P. Sharma, Congo red dye adsorption onto cationic amino-modified walnut shell: Characterization, RSM optimization, isotherms, kinetics, and mechanism studies, *Groundw. Sustain. Dev.*, 2023, **21**, 100931.
66 V. Watwe, S. Kulkarni and P. Kulkarni, Development of dried uncharred leaves of Ficus benjamina as a novel adsorbent for cationic dyes: Kinetics, isotherm, and batch optimization, *Ind. Crops Prod.*, 2023, **195**, 116449.
67 H. Jiang, Y. Cao, F. Zeng, Z. Xie and F. He, A Novel Fe_3O_4/Graphene Oxide Composite Prepared by Click Chemistry for High-Efficiency Removal of Congo Red from Water, *J. Nanomater.*, 2021, **2021**, 9716897.
68 I. Langmuir, The adsorption of gases on plane surfaces of glass, mica and platinum, *J. Am. Chem. Soc.*, 1918, **40**, 1361–1403.
69 A. Boehncke, G. Koennecker, I. Mangelsdorf and A. Wibbertmann, *Concise international chemical assessment document 6*, 1999.
70 Codex Alimantarius, CXS 193-1995, 2019.
71 N. Rahmanian, S. H. B. Ali, M. Homayoonfard, N. J. Ali, M. Rehan, Y. Sadef and A. S. Nizami, Analysis of Physiochemical Parameters to Evaluate the Drinking Water Quality in the State of Perak, Malaysia, *J. Chem.*, 2015, **2015**, 716125.
72 WHO, Water Guidelines – Chemical Facts, 2010.
73 H. Xue, X. Wang, Q. Xu, F. Dhaouadi, L. Sellaoui, M. K. Seliem, A. Ben Lamine, H. Belmabrouk, A. Bajahzar, A. Bonilla-Petriciolet, Z. Li and Q. Li, Adsorption of methylene blue from aqueous solution on activated carbons and composite prepared from an agricultural waste biomass: A comparative study by experimental and advanced modeling analysis, *Chem. Eng. J.*, 2022, **430**, 132801.
74 Z. Li, H. Hanafy, L. Zhang, L. Sellaoui, M. Schadeck Netto, M. L. S. Oliveira, M. K. Seliem, G. Luiz Dotto, A. Bonilla-Petriciolet and Q. Li, Adsorption of congo red and methylene blue dyes on an ashitaba waste and a walnut shell-based activated carbon from aqueous solutions: Experiments, characterization and physical interpretations, *Chem. Eng. J.*, 2020, **388**, 124263.
75 H. Wang, Z. Li, S. Yahyaoui, H. Hanafy, M. K. Seliem, A. Bonilla-Petriciolet, G. Luiz Dotto, L. Sellaoui and Q. Li, Effective adsorption of dyes on an activated carbon prepared from carboxymethyl cellulose: Experiments, characterization and advanced modelling, *Chem. Eng. J.*, 2021, **417**, 128116.
76 L. Chen, Y. Zhu, Y. Cui, R. Dai, Z. Shan and H. Chen, Fabrication of starch-based high-performance adsorptive

Open Access Article. Published on 13 September 2023. Downloaded on 1/31/2026 1:12:25 PM.
This article is licensed under a Creative Commons Attribution-NonCommercial 3.0 Unported Licence.

hydrogels using a novel effective pretreatment and adsorption for cationic methylene blue dye: Behavior and mechanism, *Chem. Eng. J.*, 2021, **405**, 126953.

77 J. Ai, H.-R. Tian, X. Min, Z.-C. Wang and Z.-M. Sun, A fast and highly selective Congo red adsorption material based on a cadmium-phosphonate network, *Dalton Trans.*, 2020, **49**, 3700–3705.

78 A. Extross, A. Waknis, C. Tagad, V. V. Gedam and P. D. Pathak, Adsorption of congo red using carbon from leaves and stem of water hyacinth: equilibrium, kinetics, thermodynamic studies, *Int. J. Environ. Sci. Technol.*, 2023, **20**, 1607–1644.

79 N. F. Al-Harby, E. F. Albahly and N. A. Mohamed, *Polymers*, 2021, **13**, 4446.

80 R. Azhdari, S. M. Mousavi, S. A. Hashemi, S. Bahrani and S. Ramakrishna, Decorated graphene with aluminum fumarate metal organic framework as a superior non-toxic agent for efficient removal of Congo Red dye from wastewater, *J. Environ. Chem. Eng.*, 2019, **7**, 103437.

81 D. Zewde and B. Geremew, Removal of Congo red using Vernonia amygdalina leaf powder: optimization, isotherms, kinetics, and thermodynamics studies, *Environ. Pollut. Bioavailability*, 2022, **34**, 88–101.

82 X. Zhao, W. Wang, Y. Zhang, S. Wu, F. Li and J. P. Liu, Synthesis and characterization of gadolinium doped cobalt ferrite nanoparticles with enhanced adsorption capability for Congo Red, *Chem. Eng. J.*, 2014, **250**, 164–174.

 © 2023 The Author(s). Published by the Royal Society of Chemistry